JOURNAL OF SPACECRAFT AND ROCKETS
Vol. 35, No. 2, March–April 1998, Pages 212-224

Analysis of the TOPEX/Poseidon Operational Orbit: Observed Variations and Why

Raymond B. Frauenholz,* Ramachandra S. Bhat,† and Bruce E. Shapiro†
Jet Propulsion Laboratory, California Institute of Technology, Pasadena, California 91109-8099
and
Robert K. Leavitt‡
Sterling Software, Inc., Pasadena, California 91107-4230

Following launch on Aug. 10, 1992, TOPEX/Poseidon began a very successful global study of the Earth's ocean circulation using a combination of dual-frequency radar altimetry and precision orbit determination. The 1336-km nearly circular frozen orbit and 10-day repeat ground track have been closely monitored and accurately controlled using precise mean orbital elements. A new osculating-to-mean conversion technique designed specifically to meet the stringent TOPEX/Poseidon orbit control requirements removes all short- and long-periodic geopotential and third-body gravity perturbations acting over 10 days. The most important orbital parameter, mean semimajor axis, demonstrates stability and consistency to 13 cm rms using a 20 × 20 geopotential field. The mean semimajor axis exhibits unique behavior with intervals of either orbital boost or deboost induced by along-track forces of body-fixed origin that change magnitude and direction depending on the satellite yaw-control mode and solar array articulation strategy. Nine orbit maintenance maneuvers, recently augmented by selective use of solar array articulation, have maintained the semimajor axis within ±5 m of the reference value, thereby keeping the ground track within the ±1-km equatorial longitude control band. Other orbital parameters remain within required limits without dedicated maneuvers.

Nomenclature

A/m = satellite area-to-mass ratio, varies with β' angle, m^2/kg
a = orbit mean semimajor axis, km
a_o = mean semimajor axis of reference orbit, km
C_D = satellite atmospheric drag coefficient
$\mathrm{d}a/\mathrm{d}t$ = rate of change in semimajor axis, cm/day
$\mathrm{d}V/\mathrm{d}a$ = rate of change of satellite circular velocity with respect to mean semimajor axis, mm/s/m
$\mathrm{d}V/\mathrm{d}i$ = rate of change of satellite circular velocity with respect to mean orbital inclination, m/s/deg
e = orbit mean eccentricity
e_o = mean eccentricity of reference orbit
$F_{10.7}$ = solar flux measured at 10.7-cm wavelength, 10^{-22} W/m^2/Hz
$\bar{F}_{10.7}$ = 81-day mean solar flux measured at 10.7-cm wavelength, 10^{-22} W/m^2/Hz
f = orbit true anomaly, deg
i = orbit mean inclination, deg
i_o = mean inclination of reference orbit, deg
$J_{l,m}$ = Earth tesseral harmonics of degree l and order m
M = orbit mean anomaly, deg
N = averaging interval for mean elements computation
n = $\sqrt{(\mu/a^3)}$, orbital mean motion, rad/s
$\dot{n}$ = rate of change in mean motion, rad/s^2
p = number of orbit nodal periods in a single ground-track repeat cycle
q = number of Earth rotations during a single ground-track repeat cycle relative to the precessing satellite orbit plane
t = time, days
u = orbit argument of latitude, $\omega + f$, deg
V = $\sqrt{(\mu/a)}$, satellite circular velocity, km/s
β' = angle between the orbit plane and the direction to the sun, deg
Δe = variation in eccentricity
Δf = variation in true anomaly, deg
Δt = time increment, s
$\Delta\lambda$ = equatorial longitude offset from reference ground-track value, km
μ = central body gravitational constant, km^3/s^2
ρ = atmospheric density, kg/km^3
ω = orbit mean argument of perigee (AOP), deg
$\dot{\omega}$ = rate of change in AOP, deg/s
ω_e = Earth rotation rate, rad/s
ω_o = mean AOP of reference orbit, deg

Received Nov. 6, 1995; revision received Oct. 10, 1997; accepted for publication Oct. 20, 1997. Copyright © 1990 by the American Institute of Aeronautics and Astronautics, Inc. The U.S. Government has a royalty-free license to exercise all rights under the copyright claimed herein for Governmental purposes. All other rights are reserved by the copyright owner.

*Program/Project Manager I, Navigation and Flight Mechanics Section.
†Senior Member of Engineering Staff, Navigation and Flight Mechanics Section.
‡Principal Member of Professional Staff, Navigation and Flight Mechanics Section.

Introduction

THE Ocean Topography Experiment (TOPEX/Poseidon) mission, a joint project of NASA and the French space agency CNES (Centre National d'Etudes Spatiales), has completed its three-year primary mission and is now conducting an extended mission phase. Early mission and orbit design investigations by Frautnick and Cutting[1] identified the need for accurate control of an exactly repeating satellite ground track to meet TOPEX/Poseidon science objectives. Farless[2] later defined a detailed orbit design space from which the operational orbit was ultimately selected. The reference orbit provides an exact repeat ground track covering 127 orbits over 10 sidereal days phased to overfly two verification sites supporting onboard altimeter calibration activities.

Maneuver design[3] prior to launch indicated that precise mean orbital elements were necessary to monitor and control the ground track within ±1 km of the fixed 10-day repeat reference track. As of July 4, 1997, a total of 176 repeat cycles were completed, and 9 orbit maintenance maneuvers (OMMs) had been performed since first achieving the operational orbit on Sept. 23, 1992. By this time the satellite had completed 22,352 orbits, and only 95 nodal crossings (~0.4%) had fallen outside the ground-track control band.

Precision orbit determination (POD) performed by the NASA Goddard Space Flight Center (GSFC) using laser-ranging measurements and tracking data acquired by the CNES tracking system

DORIS (Doppler orbitography and radiopositioning integrated by satellite) define geocentric radial position to an unprecedented accuracy of ~4 cm rms (Ref. 4). Second-generation orbit analyses reduce this uncertainty to under 3 cm by incorporating many modeling improvements, including new tidal models.[5] Definitive ephemerides from the POD process have been used to reconstruct the operational orbit history in terms of precise classical mean elements. This paper describes the method used to compute mean elements, establishes their accuracies, and identifies the major perturbing forces affecting their observed variations and the resulting effects on the satellite ground track.

Operational Orbit

The reference mean elements define a nearly circular frozen orbit with a mean altitude of ~1336 km and an orbital period of ~112 min. The mean semimajor axis a_o and inclination i_o (Table 1) define an Earth-fixed reference ground track with a 10-day repeat cycle phased to overfly two altimeter verification sites. The frozen orbit restricts the variation in orbital eccentricity and argument of perigee (AOP), thereby limiting satellite altitude variability to enhance altimetry performance while also eliminating the need for dedicated maneuvers to control these orbital parameters. The 66-deg orbit is near the critical inclination (~63.4 deg) where J_2 contributions to $\dot{\omega}$ are nearly zero. Frozen orbit conditions result from balancing secular perturbations of the even zonal harmonics with long-period perturbations of the odd zonal harmonics.[6–9] A geopotential field of at least 13×13 was needed to design the frozen orbit for TOPEX/Poseidon.[10] However, the final orbit design uses a 20×20 geopotential model to provide computational stability of the mean semimajor axis to much better than a centimeter. The technique used to achieve this accuracy is described later in the paper.

Accurate knowledge of the mean semimajor axis is critical to effective control of the orbit and ground track. Departure of the actual ground track from the reference value results from along-track forces that perturb the mean semimajor axis, changing the orbital period by 1.3 ms for each meter of semimajor axis change. This period change induces an equatorial longitude drift rate of ~0.6 m per orbit relative to the reference track, ~76 m during a single 127-orbit repeat cycle, totaling ~230 m after 30 days. Although maintaining the ground track within the ±1-km control band, the mean semimajor axis has been controlled within ±5 m of a_o throughout the mission. These maneuvers, performed near the eastern control boundary, raise the mean semimajor axis from a few meters below a_o to a few meters above. This strategy has utilized nine OMMs since launch to maintain ground-track control while also keeping all orbital parameters within their required limits. The frozen orbit ensures that the mean eccentricity remains an order of magnitude smaller than needed for effective altimetry ($e \leq 0.001$). Periodic inclination variations of less than ~4 m deg about i_o ensure required ground-track control without dedicated maneuvers.

The accuracy of the mean orbital parameters depends on both orbit knowledge and the computational technique. Effective ground-track control requires a stable mean semimajor axis known to better than 1 m. Operational orbit determination, provided by the GSFC Flight Dynamics Facility (FDF), uses primarily one-way Doppler acquired via the NASA Tracking and Data Relay Satellite System (TDRSS).[11] The FDF determines satellite state vectors from which osculating elements are defined. Mean elements are then computed from these osculating elements. The determination accuracy of the mean semimajor axis is ~45 cm (3σ), whereas the osculating-to-mean conversion error (described later) is ~40 cm (3σ). Combined,

Table 1 Reference mean elements and orbit determination performance for the operational orbit

Orbital parameters	Reference values	3σ orbit determination requirements	Achieved 3σ OD accuracies
a_o, km	7714.42938	1 m	45 cm
i_o, deg	66.0408	1 m deg	0.05 m deg
e_o, ppm	95	10	0.75
ω_o, deg	90	$u = 5$ m deg	$u < 1$ m deg

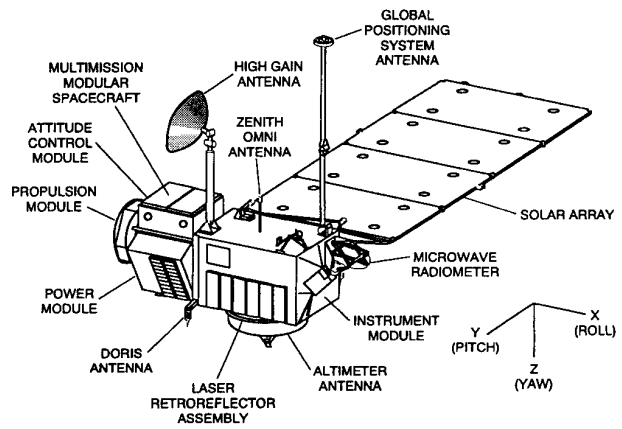

Fig. 1 TOPEX/Poseidon satellite.

these error sources define a total uncertainty of ~60 cm (3σ); required accuracy is 1 m.

It was known prior to launch that deviations from the ideal ground track would result from the combined effects of lunar and solar gravity and atmospheric drag. Soon after launch, additional, unexpected, along-track forces were observed that are attitude dependent. Understanding their behavior and the effects on the orbit and ground track requires knowledge of the satellite attitude control and solar-array articulation strategies.

Satellite Characteristics

The TOPEX/Poseidon is a three-axis stabilized satellite (Fig. 1); the roll (X), pitch (Y), and yaw (Z) axes are controlled to ensure that the altimeter antenna and large solar array (25.5-m^2 area) maintain accurate pointing. The satellite pitches at once per orbit rate to maintain nadir pointing, whereas "yaw-steering" about the nadir direction keeps the solar array pointed near the sun for power management. In addition, the solar array continuously pitches to track the sun using a fixed pitch offset from the solar normal to limit peak battery-charging currents. The pitch offset, currently 50.5 deg, can be applied to either lead or lag the ever-changing solar normal position.

A key parameter governing the attitude control algorithm is the angle β', which is positive when the sun is above the orbit plane and negative when it is below the orbit plane. The β' angle varies sinusoidally between positive and negative extremes over periods of ~56 days. Variations over a year result in peak absolute values as large as ~88 deg.

The satellite yaw-steers when $|\beta'| > \sim 15$ deg. The yaw-steering motion causes the satellite's Y axis to swing back and forth across the satellite's flight path. When $\beta' > +15$ deg, the satellite performs "positive yaw-steering," whereas "negative yaw-steering" is employed when $\beta' < -15$ deg. Near $\beta' \simeq 15$ deg, the satellite is commanded to a "fixed-yaw" position to avoid excessive yaw angular rates. The satellite attitude is maintained at a zero yaw angle when $0 < \beta' \leq 15$ deg; in this attitude the satellite "flies forward" with the $+X$ axis pointed along-track in the direction of motion. When $-15 \leq \beta' < 0$ deg, the satellite "flies backward" in a 180-deg yaw position with the $-X$ axis pointed in the direction of motion. A 180-deg yaw flip maneuver performed near $\beta' = 0$ keeps the solar array in sunlight.

Mean Orbital Elements

The 1-m accuracy requirement placed on the mean semimajor axis dictates the mean elements' definition and computational technique. Most osculating-to-mean element conversion techniques follow the methods of Kozai[12] or Brouwer[13] in which the short-periodic perturbations present in the osculating elements are removed to obtain mean elements. The dominant contributor to these perturbations comes from J_2, and mean elements are obtained by subtracting the J_2 short-periodic perturbations from the osculating elements. For TOPEX/Poseidon, the true semimajor axis oscillates about the mean with an amplitude of ±7.2 km. This amplitude reduces to ±80 m by removing the short-periodic perturbations present in a 2×2 geopotential field, which includes J_2.

In response to the need for the 1-m accuracy requirement, Guinn[14] developed a new technique to compute precise mean elements for near-circular orbits. This technique defines an intermediate orbit lying between the Kozai and secular orbits obtained by removing both short- and long-periodic perturbations from the osculating elements. The periodic perturbations due to Earth, lunar, and solar gravitational harmonics are averaged over N days to obtain stable mean elements. This process ignores the relatively small effects of nongravitational perturbations such as solar radiation pressure and atmospheric drag. The appropriate value of N depends on the orbital characteristics, mission accuracy requirements, and necessary computational accuracy.

The computational process is iterative. The periodic perturbations are calculated using osculating elements to compute mean elements from which new osculating elements are then defined. This process repeats until the original osculating elements are recovered within an acceptable tolerance. Tolerances for individual orbital parameters are chosen consistent with needed computational accuracy, which is dependent primarily on the geopotential field size used for averaging. The osculating-to-mean conversion software based on Guinn's procedure (OSMEAN)[15] provides options for selecting geopotential field size, third-body effects, and the number of days (N) over which the periodic perturbations are averaged.

The effects of periodic geopotential perturbations are expected to average out during a single 10-day ground-track repeat cycle. Therefore, a 10-day averaging interval became a reasonable candidate value for N. The POD process used the 70 × 70 Joint Gravity Model-2 (JGM-2) (Ref. 16) to generate precision orbit ephemerides (POEs) for the first 100 ground-track repeat cycles. These and all subsequent cycles have been reprocessed using an upgraded JGM-3 (Ref. 17), which is also a 70 × 70 model. Operational navigation continues to use the JGM-2 model. However, it is computationally prohibitive to use the full 70 × 70 field to perform operational navigation tasks, and this is not necessary to meet the orbit determination and control requirements. Resonances arise when the satellite completes p nodal periods while the Earth rotates q times relative to the precessing satellite orbit plane, and thus geopotential terms that are near multiples of p/q (127/10) contribute significant secular forces. A 13 × 13 truncation of the JGM-2 gravity field includes first-order, near-resonant terms, whereas a 26 × 26 truncation includes both first- and second-order terms. The mean semimajor axis is stable and consistent to less than 1 cm using the 26 × 26 field and lunar and solar gravity over a 10-day interval. Accordingly, this 26 × 26 model was adopted as a convenient reference truth model to evaluate mean-element computational accuracy.

A representative sample accuracy evaluation uses osculating state vectors from the POE between March 3 and 23, 1994 (repeat cycles 54 and 55). Mean elements were computed using 2 × 2, 10 × 10, 13 × 13, 17 × 17, and 20 × 20 truncations of JGM-2 with a 10-day averaging interval while also removing the effects of lunar and solar gravity. These mean elements were then compared with those obtained using the 26 × 26 truth model. The semimajor axis requires a 20 × 20 geopotential field to reduce the computational errors to a negligible level (<1 cm) (Fig. 2a), whereas the other orbital parameters achieve satisfactory accuracy levels using smaller fields (Fig. 2b).

The periodic variations in osculating semimajor axis of ±7.2 km about the true mean during each orbital period are dramatically reduced to ±80 m by removing the effects of J_2 (Fig. 3a). The rms error relative to the 26 × 26 gravity field is reduced to 144 cm by removing perturbations present in a 10 × 10 field and to 41 cm using a 13 × 13 field (Fig. 3b). The rms error is reduced further to 10 and 0.6 cm by removing the perturbations in the 17 × 17 and 20 × 20 gravity fields (Fig. 3c). Accordingly, a 20 × 20 truncation of the JGM-2 model was adopted for computing mean elements. Operational navigation tasks shared by the GSFC/FDF and the Jet Propulsion Laboratory (JPL) also use this gravity field for all orbital computations.

First-order, near-resonant tesseral harmonics determine the minimum averaging period (N) required to obtain a consistent mean semimajor axis. The tesseral harmonics $J_{\ell,m}$, with ℓ in the range of 13–19 and m with values 12 and 13, cause significant variations in semimajor axis with periods of 1.42 and 3.31 days (Table 2). Obtaining consistent values of mean semimajor axis requires removal of these perturbations by averaging over the maximum period of these variations.

Table 2 Near-resonant tesseral harmonic perturbations in mean semimajor axis

Tesseral harmonics, $J_{\ell,m}$	Amplitude, m	Period, days
$J_{13,12}$	1.17	1.42
$J_{12,13}$	1.46	3.31
$J_{15,12}$	0.05	1.42
$J_{15,13}$	0.51	3.31
$J_{17,12}$	0.15	1.42
$J_{17,13}$	0.16	3.31
$J_{19,12}$	0.02	1.42
$J_{19,13}$	0.08	3.31

Table 3 Achieved mean element computational accuracies (20 × 20 geopotential plus lunar and solar gravity averaged over 10 days)

Orbital parameters	3σ computational accuracies
a	40 cm
i	1.5 m deg
e	21 ppm
ω	27 deg

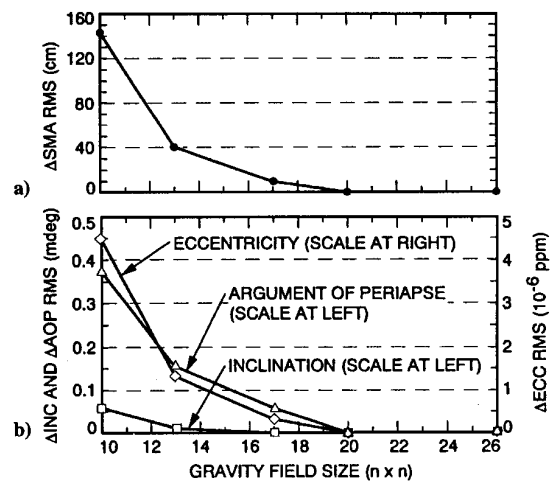

Fig. 2 Mean element computation accuracy relative to 26 × 26 gravity field (removal of third-body gravity acting over 10 days).

To illustrate this averaging process, mean elements were computed using different values of N. The reference for comparison is the 20 × 20 gravity field averaged over 10 days, the duration of one ground-track repeat cycle. The amplitude of the semimajor axis varies ±30 m about the 10-day mean (Fig. 4a) when averaging over just one orbit (~112 min). This amplitude is reduced to ±2.2 m when averaging over one day, which still includes sizable perturbations having periods of 1.42 and 3.31 days (Fig. 4b). Averaging over two days removes the perturbations having a 1.42-day period, reducing the computational error to about 1 m. Averaging over at least 3.31 days removes the remaining resonances, totally eliminating computational errors with respect to the 10-day reference.

Although there are no long-periodic perturbations in a due to lunar and solar gravity, these third-body forces induce short-periodic fluctuations in a due to long-periodic variations in n and i. The amplitudes of these fluctuations vary up to ~150 cm over a period of 11.2 days, with lunar gravity the dominant contributor (Fig. 5). Because such errors in a are unacceptably large, variations in the mean orbital elements due to these short-periodic perturbations must be removed. Averaging over any interval $N > 3.31$ days removes the desired geopotential and third-body perturbations. A 10-day averaging interval was adopted operationally for it provides stable mean values for all orbital parameters and is computationally efficient.

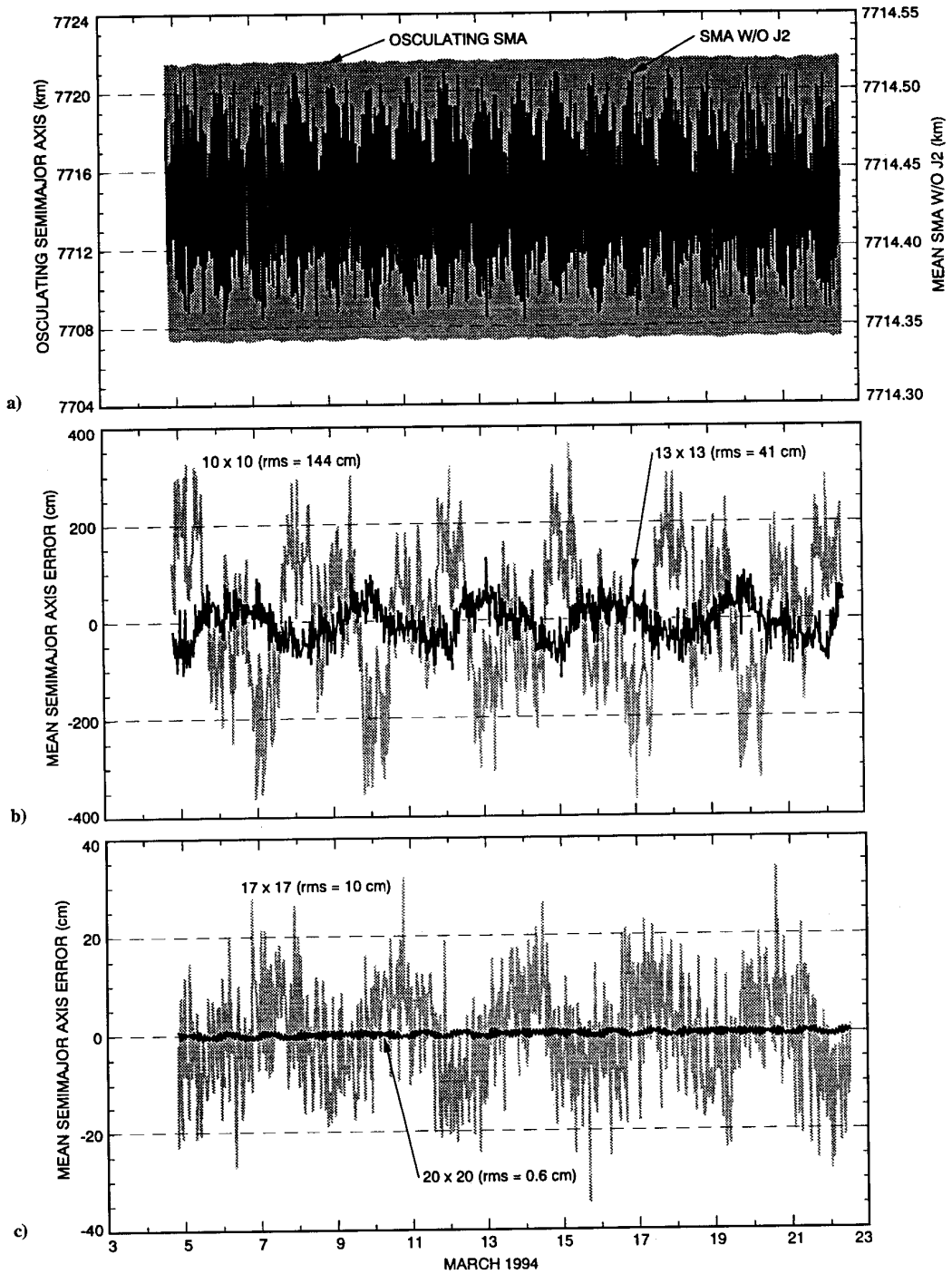

Fig. 3 Mean semimajor axis computation accuracy relative to 26 × 26 gravity field (removal of geopotential and third-body gravity acting over 10 days).

The foregoing results are consistent with the theoretical assessment[3] that mean elements should be computed by removing the short- and long-term perturbations present in a 20 × 20 geopotential field and lunar and solar gravity, each acting over a 10-day period. Accuracies were assessed based on the stable behavior of the mean orbital elements over two 10-day ground-track repeat cycles sampled every 4 min. Table 3 lists the computational accuracies for the key orbital parameters. Most notable is the mean semimajor axis, with a stability and consistency of ±40 cm (3σ).

Semimajor Axis

Prelaunch studies indicated that the primary perturbation affecting the mean semimajor axis would be atmospheric drag.[3] The accumulated semimajor axis decay could be removed to control the ground track. Accordingly, the drag-induced semimajor axis decay rate for this near-circular orbit [Eq. (1)][18] was expected to depend primarily on the A/m and ρ, which itself is a strong function of $F_{10.7}$ (Ref. 19):

$$\frac{\mathrm{d}a}{\mathrm{d}t} = -\rho C_D \frac{A}{m}\sqrt{\mu a}\left(1 - \frac{\omega_e \cos i}{n}\right)^2 \tag{1}$$

The satellite variable mean area (VMA; the per-orbit average projected area at a given β'; model defined by table of VMA vs β') projected in the along-track direction ranges from ~9 m^2 at peak β' to ~22 m^2 at minimum β'. As a result, the mean A/m for this 2406-kg satellite varies between ~0.004 and ~0.009 m^2/kg. Figure 6 describes $\mathrm{d}a/\mathrm{d}t$ for these two A/m extremes in terms of

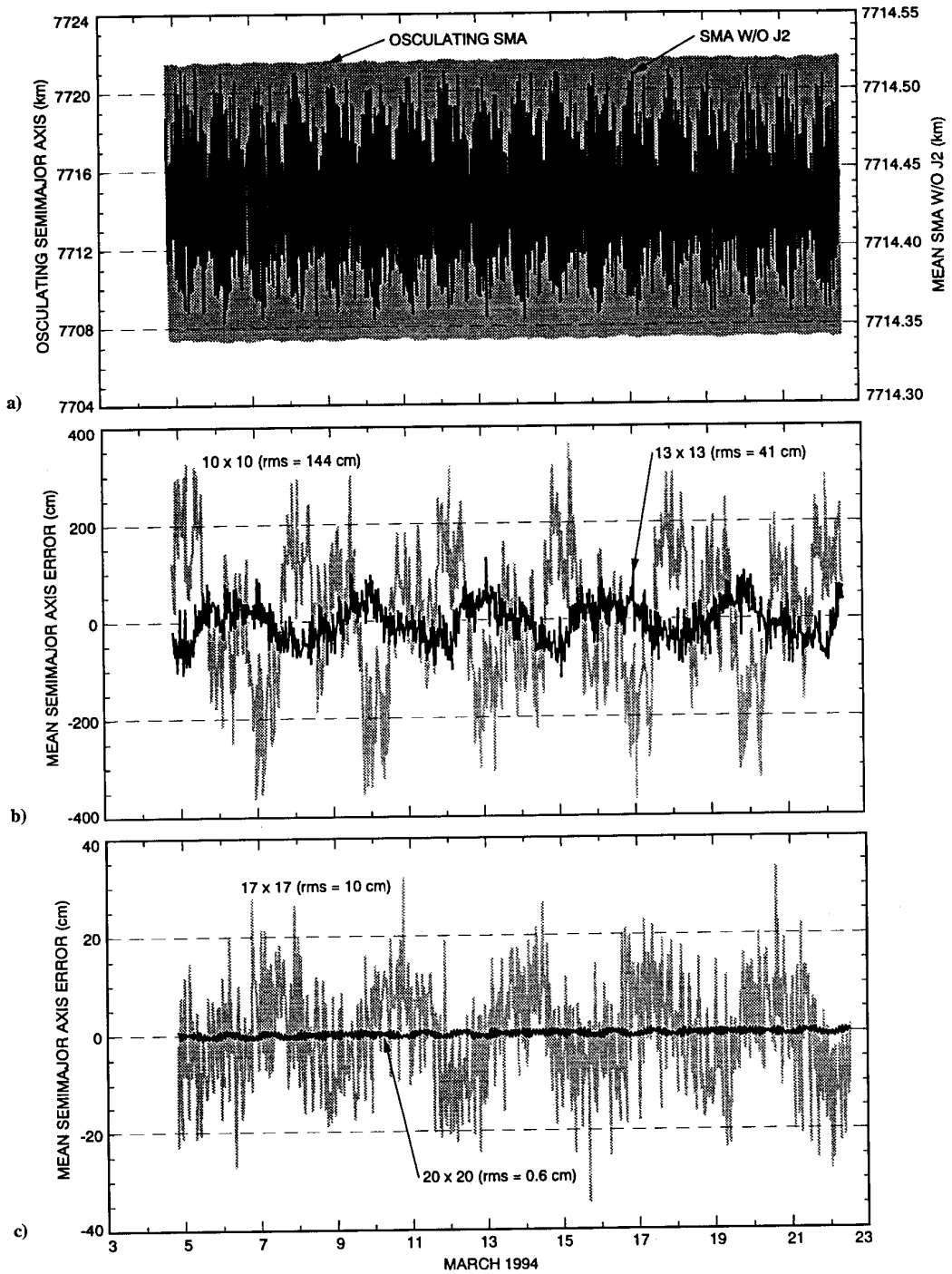

Fig. 3 Mean semimajor axis computation accuracy relative to 26 × 26 gravity field (removal of geopotential and third-body gravity acting over 10 days).

The foregoing results are consistent with the theoretical assessment[3] that mean elements should be computed by removing the short- and long-term perturbations present in a 20 × 20 geopotential field and lunar and solar gravity, each acting over a 10-day period. Accuracies were assessed based on the stable behavior of the mean orbital elements over two 10-day ground-track repeat cycles sampled every 4 min. Table 3 lists the computational accuracies for the key orbital parameters. Most notable is the mean semimajor axis, with a stability and consistency of ±40 cm (3σ).

Semimajor Axis

Prelaunch studies indicated that the primary perturbation affecting the mean semimajor axis would be atmospheric drag.[3] The accumulated semimajor axis decay could be removed to control the ground track. Accordingly, the drag-induced semimajor axis decay rate for this near-circular orbit [Eq. (1)][18] was expected to depend primarily on the A/m and ρ, which itself is a strong function of $F_{10.7}$ (Ref. 19):

$$\frac{\mathrm{d}a}{\mathrm{d}t} = -\rho C_D \frac{A}{m}\sqrt{\mu a}\left(1 - \frac{\omega_e \cos i}{n}\right)^2 \tag{1}$$

The satellite variable mean area (VMA; the per-orbit average projected area at a given β'; model defined by table of VMA vs β') projected in the along-track direction ranges from ~9 m^2 at peak β' to ~22 m^2 at minimum β'. As a result, the mean A/m for this 2406-kg satellite varies between ~0.004 and ~0.009 m^2/kg. Figure 6 describes $\mathrm{d}a/\mathrm{d}t$ for these two A/m extremes in terms of

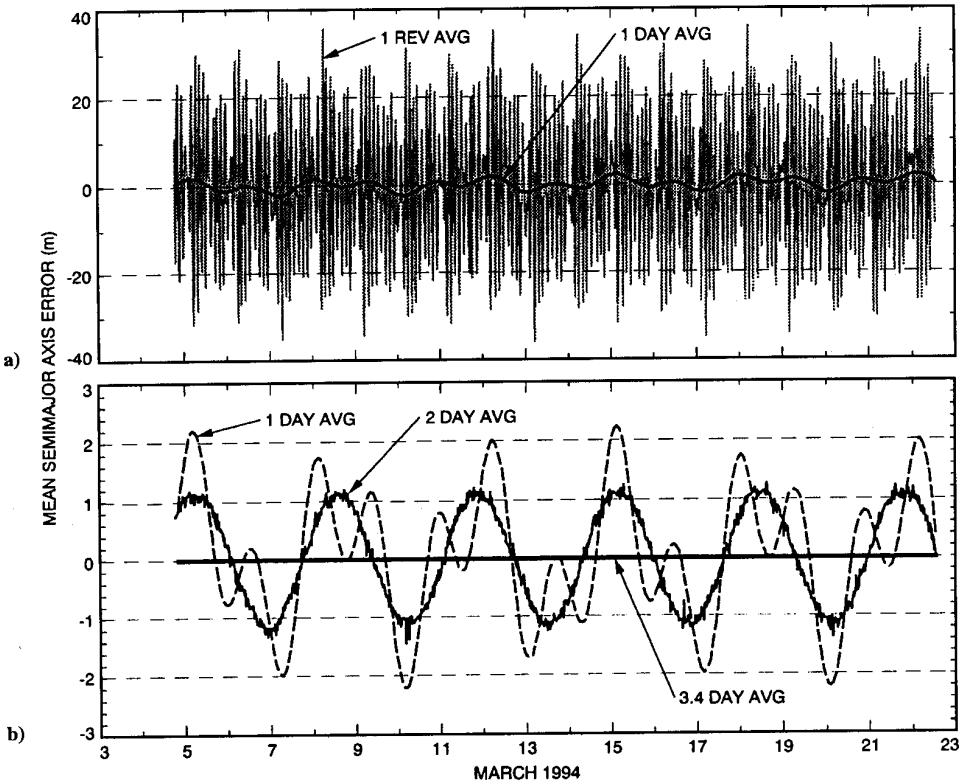

Fig. 4 Effect of averaging interval on mean semimajor axis computation accuracy for 20 × 20 gravity field (includes removal of third-body gravity perturbations).

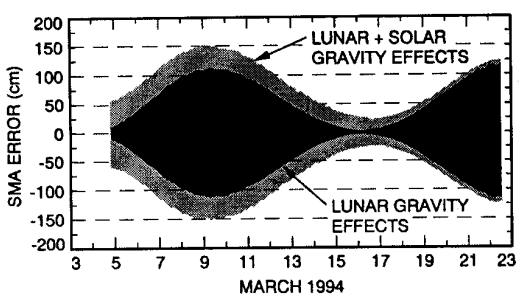

Fig. 5 Effects of lunar and solar gravity on mean semimajor axis computation accuracy.

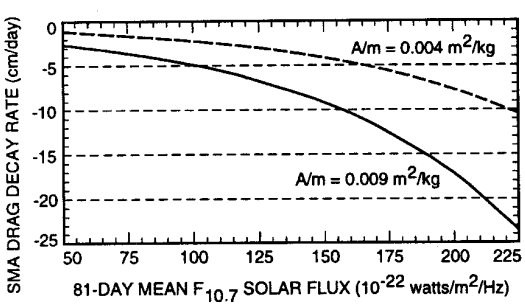

Fig. 6 Predicted semimajor axis decay rate due to drag.

$\bar{F}_{10.7}$. The $\bar{F}_{10.7}$ has dropped from ~125 to ~70 × 10^{-22} W/m²/Hz between launch and the fall of 1996, when solar cycle 22 ended, and thus da/dt has varied between ~1 and ~7 cm/day.

Observed Semimajor Axis

Figure 7 shows the mean semimajor axis history for 176 repeat cycles ending on July 4, 1997. Nine OMMs were performed during this period. Each OMM was performed near the eastern ground-track control band, raising the mean semimajor axis above a_o and reversing the ground-track drift from east to west. Typical OMMs are ~3–4 mm/s in the along-track direction ($dV/da \simeq 0.466$ mm/s per meter).

The expected monotonic decay in semimajor axis due to just atmospheric drag was not always observed. Instead, the semimajor axis sometimes increased, indicating the presence of additional along-track forces now confirmed to have body-fixed origins.[20] Theoretical models[21–23] define the body-fixed forces for each yaw-control mode based on estimates of satellite and solar array surface properties and in-flight temperature measurements. During yaw steering, only forces originating from the satellite's Y axis map into the along-track direction. Such forces can result from misalignment and curling of the solar array due to temperature differences between the front and rear surfaces. During fixed yaw, along-track forces originate only from the X axis due to the presence of a solar-array pitch offset.

Figure 8 depicts the effect of typical body-fixed forces on the rate of change in mean semimajor axis during each yaw-control mode for the full range of β' angles. The semimajor axis increases during negative yaw steering ($\beta' < -15$ deg), whereas positive yaw steering causes decreases. Flying forward in fixed yaw ($\beta' > +15$ deg) increases the semimajor axis, whereas flying backward results in decreases. The magnitude of da/dt is about three times larger during fixed yaw compared with that during yaw steering, and use of a lead or lag solar-array pitch offset dictates the direction. These forces are equal to or greater than those caused by atmospheric drag. In-flight estimates of these body-fixed forces and an accurate predictive model were needed to monitor the mean semimajor axis effectively and to design maneuvers for ground-track control.

Atmospheric Drag vs Body-Fixed Forces

The effects of body-fixed forces on the mean semimajor axis are independently estimated by two different operational orbit determination processes. The TDRSS-based solutions provided by the GSFC/FDF estimate a single along-track thrust parameter acting over a tracking arc length of at least four days. This estimate is obtained in the presence of all nongravitational forces, including nominal drag and direct solar radiation pressure. The equivalent

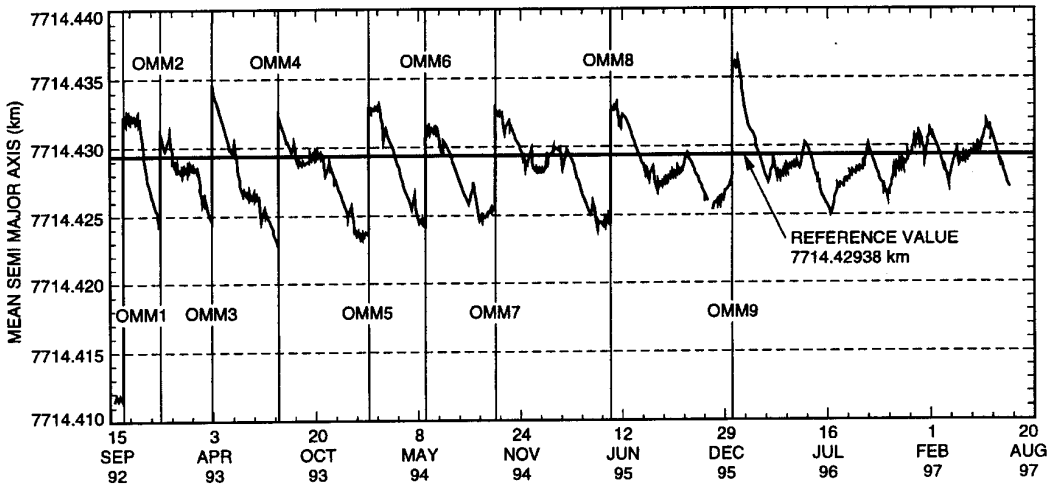

Fig. 7 Mean semimajor axis history based on a 20 × 20 gravity field.

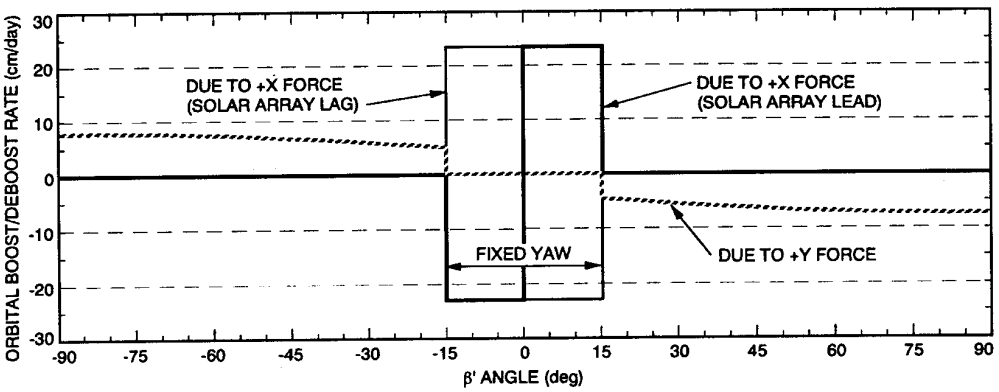

Fig. 8 Typical daily changes in da/dt vs β' due to body-fixed forces for each yaw-control mode.

thrust acceleration defines the total rate of change in the semimajor axis at the center of the tracking arc. (For this orbit, an along-track acceleration of 1 nm/s^2 induces a rate of change in semimajor axis of ~18.5 cm/day.) In a separate process primarily intended to validate POEs, daily quick-look orbit determination[24] based on precise laser-ranging measurements and global positioning system (GPS) data includes estimates of the total once-per-orbit, along-track nongravitational acceleration. Isolating the contribution to da/dt induced by the body-fixed forces requires removal of drag effects, as defined by Eq. (1). The integrity of these two independent estimation processes greatly depends on the accuracy of the atmospheric density model. Operational navigation tasks shared by the GSFC/FDF and JPL use the Jacchia–Roberts[25–28] (JR) density model, which has been favorably compared with the Drag Temperature Model[29] used in the POD process, although neither model reflects flight data at the TOPEX/Poseidon altitude. Daily 30-h tracking arcs used in the quick-look process provide orbit solutions that agree very well with formal POE deliveries, but estimates of the nongravitational accelerations are sometimes inconsistent because these short-arc solutions may lack the information content necessary to estimate these accelerations confidently. However, estimates obtained from the TDRSS-based orbit solutions with at least a four-day tracking arc are generally more consistent because of the smoothing effects of the longer tracking arc. Still, these two independent estimation methods have demonstrated excellent agreement and have consequently improved confidence in the empirical prediction models required for effective ground-track control.

The yaw-steering period from March 6 to April 24, 1994, serves to illustrate the estimation process and prediction model development and to explain the mean semimajor axis behavior in terms of individual drag and body-fixed forces. Figure 7 shows that the computed mean semimajor axis during this 49-day period (between OMM5 and 6) generally exhibits the expected monotonic "drag-like" decay behavior, but the observed rate of change of ~11.7 cm/day is much larger than can reasonably be attributed to just atmospheric drag. Similar results were independently obtained by the quick-look orbit estimation method, where da/dt varies between −10 and −15 cm/day (Fig. 9). The decay rate due to drag during this period is much lower, reduced from −5 to −2 cm/day as $\bar{F}_{10.7}$ dropped from ~100 to ~ 80 $\times 10^{-22}$ W/m^2/Hz. Removing the drag effects from the total da/dt provides estimates of the body-fixed contribution. Here, the body-fixed and drag-induced forces are of similar magnitude at lower values of β', whereas the body-fixed forces dominate at higher β', especially when the orbit is in full sun ($\beta' > 55.7$ deg). Figure 9 shows an empirical model describing changes in da/dt induced by the body-fixed forces. This model defines da/dt as cubic functions of β', which has a periodic variation of ~112 days.

The individual effects of body-fixed forces and drag on the mean semimajor axis are compared in Fig. 10. Drag always induces semimajor axis decay, and the rate depends on the level of solar activity. Figure 10a shows that da/dt due to drag also exhibits periodic variations with β' as the VMA changes. The body-fixed forces vary with yaw-control mode and β' (Fig. 10b). The drag and body-fixed forces add during positive yaw-steering ($\beta' > 15$ deg), whereas they offset during negative yaw-steering ($\beta' < -15$ deg). The larger body-fixed forces during fixed yaw offer opportunities to apply small changes selectively in the mean semimajor axis by varying the β' values defining entry into or exit from fixed yaw or both, thereby altering the duration of the boost and deboost forces. Also, selective use of lead or lag solar-array pitch offset positioning allows sustained intervals of boost or deboost as needed to adjust the ground track. As is evident in Fig. 10b, this strategy has been used frequently since OMM9 in January 1996 to maintain continuous ground-track control without the aid of propulsive maneuvers.

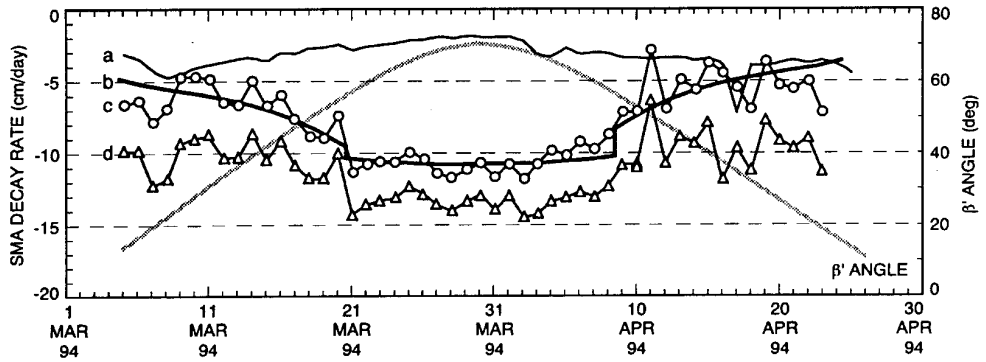

Fig. 9 Total semimajor axis decay rate due to observed nongravitational forces: a, due to drag; b, empirical model for body-fixed forces; c, due to body-fixed forces; and d, due to all nongravitational forces.

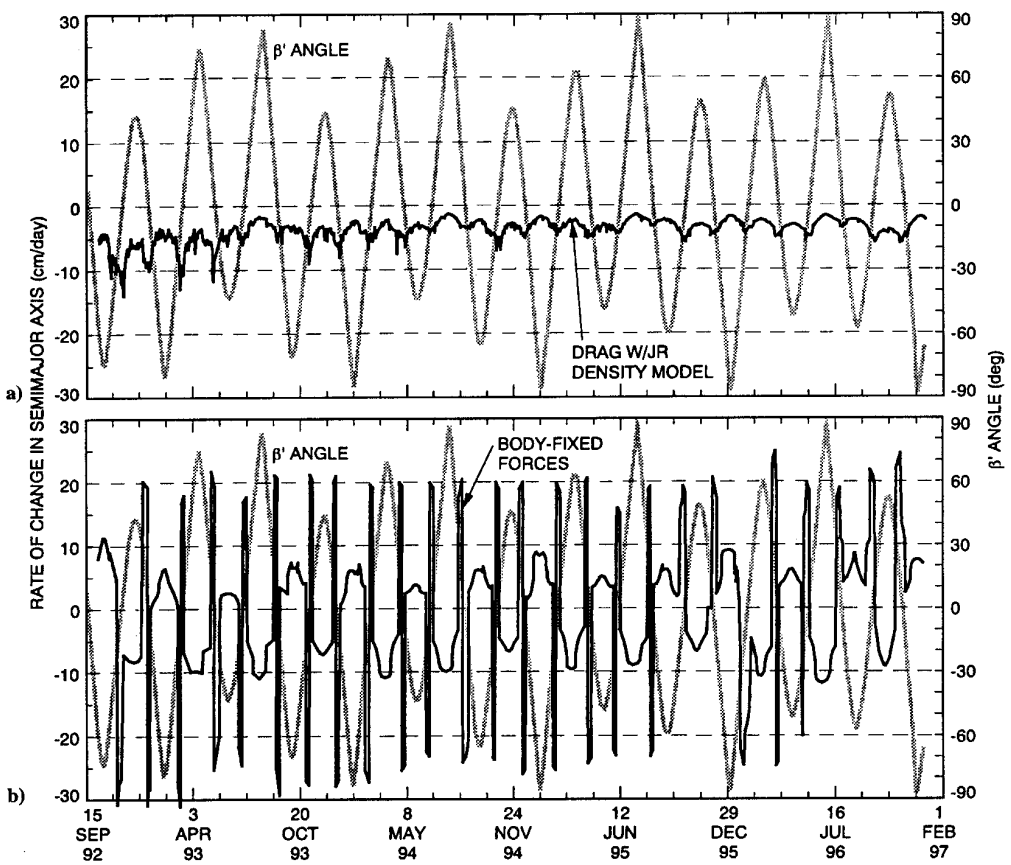

Fig. 10 Comparison of as-flown da/dt due to a) drag vs β' and b) body-fixed forces.

Effect of Body-Fixed Forces on Mean Semimajor Axis and the Satellite Ground Track

The effects of the body-fixed forces on the semimajor axis and satellite ground track were assessed by comparing trajectories with all force models active with a case in which the body-fixed forces were inactive. Figure 11 compares the mean semimajor axis values; Fig. 12 then shows the attendant effect on the ground track. With all force models active, the semimajor axis first exhibits boost followed by a sustained period of deboost at a nearly linear rate of -11.7 cm/day. Removal of the body-fixed forces results in a residual deboost rate attributable to just drag, here about -4.3 cm/day, similar to the value estimated analytically using the JR density model and daily $F_{10.7}$ observations (Fig. 9). This agreement confirms that the body-fixed and atmospheric drag forces are the dominant contributors to semimajor axis variations.

Changes in the satellite ground track due to the body-fixed forces are shown in Fig. 12 in terms of equatorial longitude differences. The comparison starts during a fixed-yaw mode when the body-fixed forces induce an orbital boost rate of ~20 cm/day. When the satellite resumes yaw-steering, the body-fixed forces abruptly change in both magnitude and direction; initially, the semimajor axis deboost rate is ~5 cm/day and gradually increases to ~10 cm/day as β' becomes larger. Without these body-fixed forces, the ground track initially drifts eastward. After resuming yaw-steering, the accumulating effect of removing the deboost forces causes the ground track to drift increasingly westward. For this example, the net integrated effect on the satellite ground track becomes significant: ~120 m in equatorial longitude after 30 days.

Effect of Solar Radiation Pressure on the Mean Semimajor Axis

Although of secondary importance in this orbit- and ground-track control problem, the effects of solar radiation pressure have been included for completeness. Solar radiation pressure has only modest effects on the mean semimajor axis and ground track because its influence averages to near zero when the orbit is in full sun ($\beta' > 55.7$ deg); the net effect during occultation periods is quite

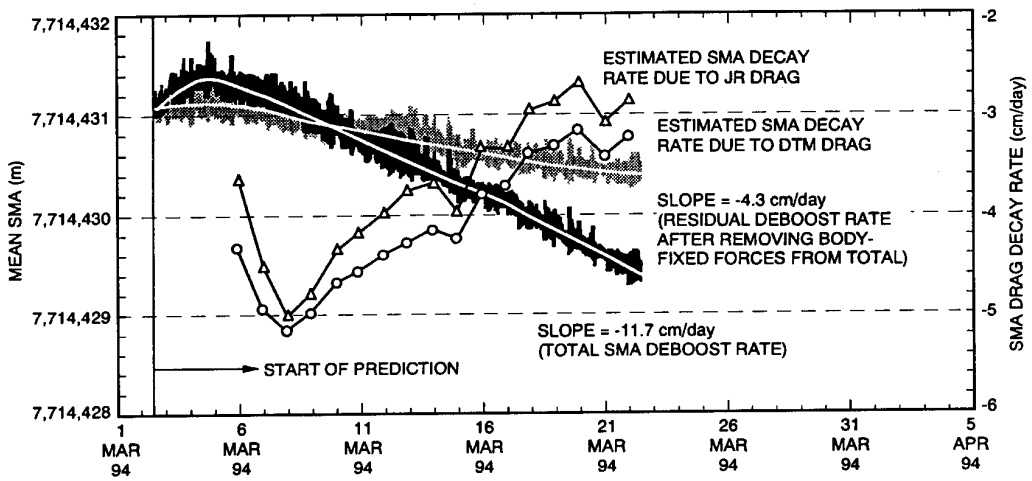

Fig. 11 Effects of body-fixed forces and drag on mean semimajor axis.

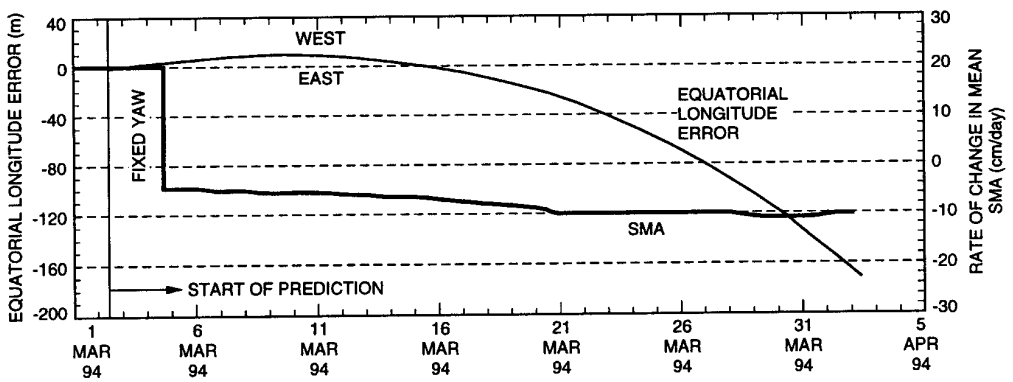

Fig. 12 Effects of body-fixed forces on satellite ground track.

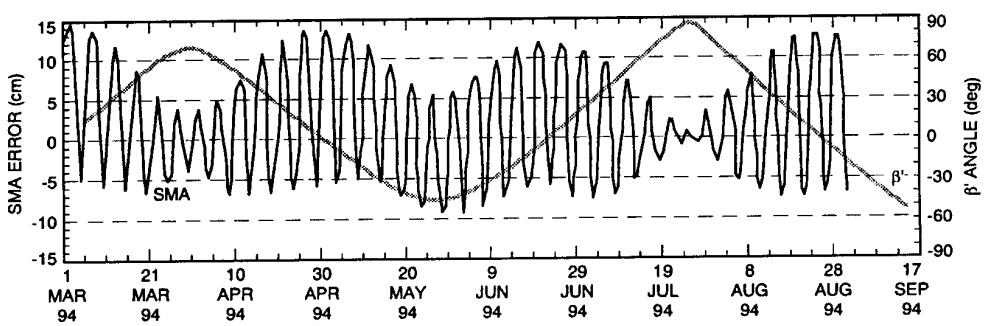

Fig. 13 Effects of solar radiation pressure on mean semimajor axis.

small compared with other perturbing forces. For example, Fig. 13 shows the effect on the mean semimajor axis for the six-month period beginning on March 1, 1994. Computed daily, differences in the mean semimajor axis exhibit periodic behavior, with peak amplitudes less than ±15 cm. The smallest errors occur during peak β' when the orbit is in full sun; the maximum errors occur near $\beta' = 0$ when the occultation intervals are longest.

Inclination

To maintain the repeating orbit and verification site overflights, the inclination must remain close to the reference value (i_o in Table 1). Prelaunch analyses[3] indicated that lunar and solar gravity perturbations cause periodic inclination variations of ±3.8 m deg about the reference value, whereas variations are negligible for nongravitational perturbations such as solar radiation pressure and atmospheric drag. The ground-track targeting procedure absorbs the effect of predicted inclination variations by adjusting the mean semimajor axis to maintain the repeating ground track within the ±1-km control band.

Observed Variations of Inclination

Since first achieving the operational orbit in September 1992, the observed mean inclination has exhibited the expected periodic variations about i_o. During 1992, the peak amplitudes of these variations were −3.3 and +3.0 m deg; more recently these amplitudes have shifted positively to −2.7 and +3.7 m deg. These variations are a combination of several clearly distinguishable periodic components of 12, 58, and 173 days. There are also very long periodic variations that have become noticeable after three years, but these amplitudes are quite small.

The major components of inclination variations are due to the third-body gravity perturbations. Figure 14 shows that the variations about i_o correlate very well with β', as does the amplitude of the periodic components. The amplitudes are higher when the orbit is in full sun ($\beta' > 55.7$ deg), whereas the mean inclination is always greater than i_o during occultation periods.

The nine OMMs implemented since September 1992, with small along-track magnitudes between 3 and 5 mm/s, have had a negligible effect on orbit inclination. Only unplanned cross-track components

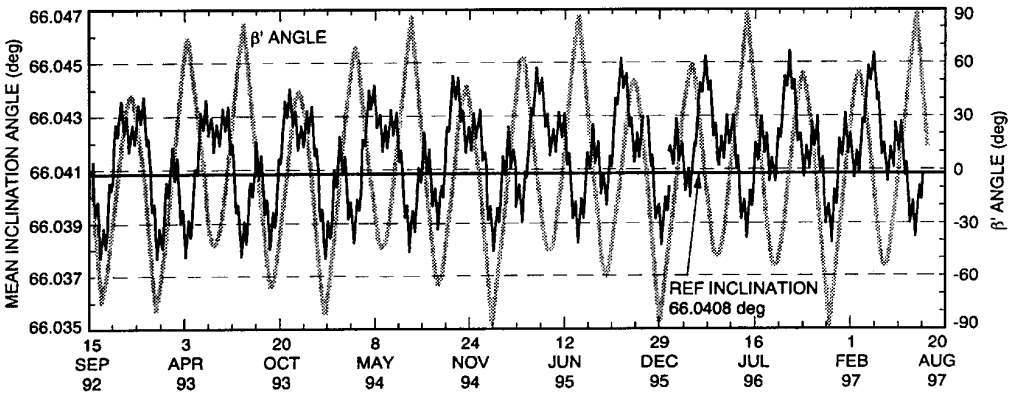

Fig. 14 Observed orbital inclination angle vs β' angle.

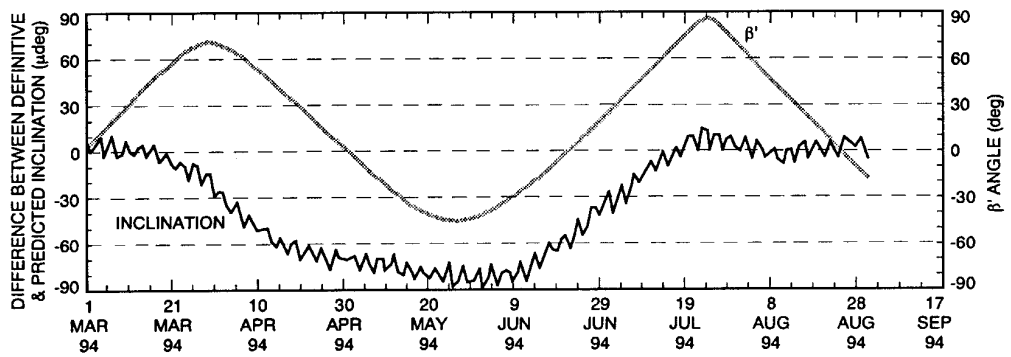

Fig. 15 Difference between definitive and predicted inclination.

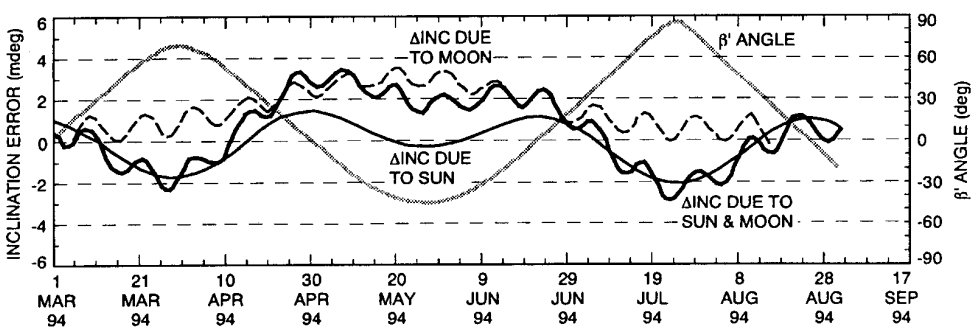

Fig. 16 Inclination variations due to lunar and solar gravity.

caused by thruster pointing errors could affect inclination, but these velocity magnitude errors are extremely small ($dV/di \simeq 125$ m/s per deg applied normal to the orbit plane).

The observed inclination includes variations due to both modeled and unmodeled perturbing forces. The behavior is predictable when unmodeled perturbations have a negligible effect. The predicted inclination during the six-month period beginning March 1, 1994, was compared with definitive values from the POE. Figure 15 shows that these inclination differences are quite small, indicating that the force models affecting inclination are well known and that inclination variations are confidently predictable.

Inclination variations due to major perturbing forces were then determined by nullifying individual force models and comparing the resulting trajectory parameters with the reference case obtained with all models active. The corresponding mean elements were differenced to isolate inclination variations.

Sun and Moon Gravitational Attraction

Prelaunch studies[3] assessed the effects of third-body gravitational perturbations on the satellite ground track from which the inclination variations were also established. The individual effects of lunar and solar gravity were first evaluated analytically and then verified using precision trajectory propagation software.

The inclination variations due to lunar gravity are dominated by the 173- and 12-day periodic components (Fig. 16 and Table 4). However, closer inspection indicates that there are also other significant periodic variations. Kaula's method[30] modified for near-circular orbits established the amplitudes and periods of four distinct components; two have amplitudes of ~0.1 and ~0.54 m deg, with periods of 12.6 and 11.7 days, respectively. In Fig. 16, these two variations appear as a single perturbation. The amplitude of the 173-day periodic component is 1.33 m deg; the other periodic component has an 87-day period and a 0.3-m deg amplitude.

There are five significant periodic components in the inclination variation induced by solar gravity. These variations are synchronized with β' (Fig. 16 and Table 4). The dominant component has an amplitude of 1.24 m deg and a period of ~59 days, about half the period of β'. One component has a period of 173 days, ~1.5 times the β' period, and an amplitude of 0.66 m deg. Two components have periods of ~87 days, or about three-quarters of the β' period, with

amplitudes of 0.35 and 0.16 m deg, respectively. The fifth component has a period of 9.3 years with an amplitude of 0.58 m deg.

The predicted size and shape of inclination variations attributed to the sun and moon are nearly identical to the observed inclination (Figs. 14 and 16), indicating that these are the dominant perturbing forces. Figure 16 shows how lunar and solar gravity perturbed the mean inclination between March and August 1994. The amplitude of these variations increases with β' for some periodic variations increase when the peak β' is higher.

Effects of Solid Earth Tides and Solar Radiation Pressure

The tidal forces induced by lunar and solar gravity cause small variations in inclination. However, they are significant here because of the stringent ground-track control requirements. The tidal effects are an order of magnitude smaller than the third-body gravity perturbations, whereas the signature is nearly identical and also a strong function of β'. Figure 17 shows the magnitude of the tidal effects varied between −0.4 and +0.3 m deg between March and August 1994.

The inclination variations due to direct solar radiation pressure (SRP) are very small and for all practical purposes may be neglected. These variations increase with β', as shown in Fig. 17. However, during full-sun periods the variations remain nearly constant; the magnitude is a function of the peak β'. The period of variation (56–59 days) is about half the β' period; the amplitude was <0.08 m deg between March and August 1994.

Table 4 Periodic inclination variations due to the sun and moon gravitational perturbations

Perturbing forces	Amplitudes, m deg	Periods of variation, days
Lunar gravity	0.10	12.6
	0.30	86.7
	0.54	11.7
	1.33	173.4
Solar gravity	0.16	86.7
	0.35	88.9
	0.58	3402.0
	0.66	173.3
	1.24	58.8 (half of β' period)

Other Forces

The inclination variations due to nongravitational forces such as atmospheric drag and body-fixed (radiation) forces are negligible. The rotating atmosphere has some effect on inclination but quite small compared with variations induced by lunar and solar gravity.

Effect of Inclination Variations on the Ground Track

The deviations in inclination from i_o affect the ground track in two ways, as shown in Fig. 18. First, the equatorial crossings slowly deviate from the reference ground track owing to inclination variations induced by third-body perturbations ($d\Delta\lambda/di \simeq 280$ m in 30 days).[31] In addition, the nodal period is a function of inclination. The maneuver-targeting process accounts for inclination-induced variations in the predicted ground track and adjusts the mean semimajor axis accordingly so that future nodal crossings remain within the control band. The signatures of inclination variation are clearly reflected in the ground track, particularly when the mean semimajor axis is within a few meters of a_o. This circumstance minimizes the ground-track drift rate relative to the reference track, especially when the ground track nears the western control boundary, as described later in the section on ground-track history.

Effect of Inclination Variations on Verification Site Overflight

Inclination errors also affect the overflight accuracy of the two verification sites, where the radius of closest approach must be maintained within ±1 km. The latitudes of both verification sites are ~35°N: the NASA site is on Harvest Platform off Pt. Conception, California, and the now-closed CNES site was near Lampedusa Island in the Mediterranean Sea. The NASA site overflight occurs on the ascending pass of orbit 22 of each repeat cycle; the CNES overflight occurred about 7 days later on the descending pass of orbit 111 of the same repeat cycle. Inclination variations cause offsets in the site overflights even when the actual nodal crossings match their reference value. A 1-m deg inclination variation causes an offset of ~74 m at these verification sites. The largest inclination variation about i_o is expected to be within ±4 m deg, resulting in an overflight offset of ±296 m. The offset increases when the nodal crossing is away from the reference node. The proximity of the ground track to the verification site depends on the nodal crossing longitude and the mean inclination. The verification site control requirement has

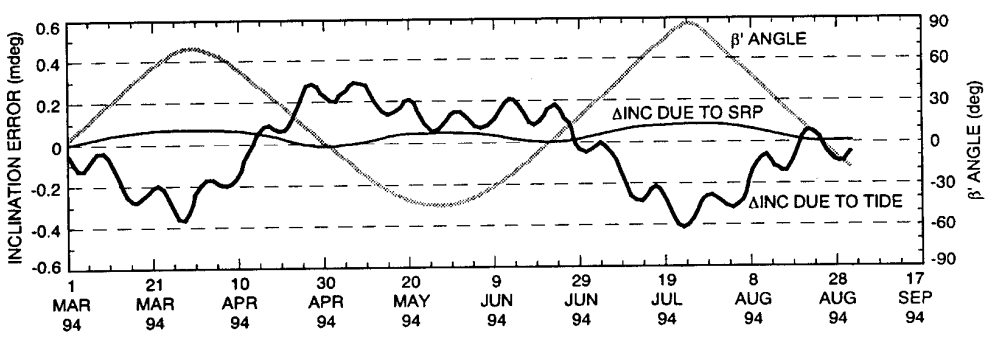

Fig. 17 Inclination variations due to tides and solar radiation pressure.

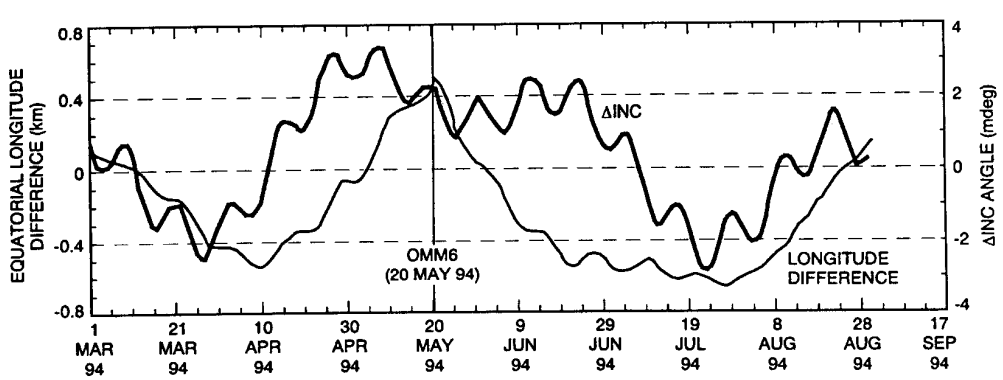

Fig. 18 Comparison of ground-track and inclination variations.

been satisfied during each OMM design by using −900 m as the western control boundary instead of −1000 m.

All control requirements have been met with the exception of five NASA site overflights. One violation was voluntary during the first repeat cycle when the ground track was still outside the western boundary and drifting slowly eastward before first entering the control band. Three involuntary overflight violations occurred during March, April, and May 1996 following OMM9 in January 1996 (Ref. 32). These overflight violations were caused by unfavorable inclination variations as the ground track came within ~150 m of the western control boundary following an attitude thruster firing anomaly shortly after OMM9, which resulted in a 46% net overburn.[33] However, the mission requirement to keep 95% of the verification site overflights within ±1 km has been comfortably met for both the NASA and CNES sites. In September 1996, the CNES site was closed, and thus these overflights are no longer monitored or controlled. Overflight monitor and control of the still-active NASA site continue.

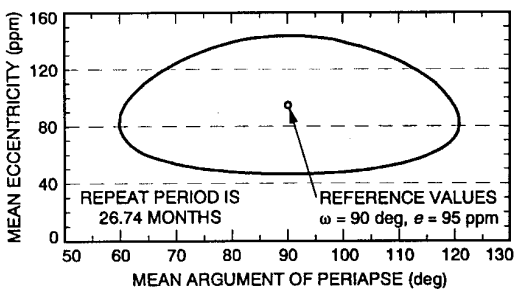

Fig. 19 Eccentricity vector (e, ω) variations for frozen orbit.

Eccentricity Vector and the Frozen Orbit

The eccentricity vector conditions achieved by the operational orbit acquisition maneuver sequence[34] were $e = 142.9$ ppm and $\omega = 90.6$ deg, compared with the target values of $e_o = 95$ ppm and $\omega_o = 90$ deg (Table 1). The closed contour shown in Fig. 19 describes the expected eccentricity vector behavior when perturbed only by a 20×20 geopotential field. This contour moves counterclockwise about the reference AOP ($\omega = 90$ deg) and has a period of 26.74 months.[35] This curve remains closed even under the influences of nongravitational perturbations such as drag and solar radiation pressure but can exhibit discontinuities resulting from in-plane maneuvers.

The achieved mean eccentricity and AOP are compared over time with the expected frozen values in Figs. 20a and 20b, respectively. This examination reveals how the small OMMs have affected e and ω variations. In Fig. 20a the observed mean eccentricity deviates somewhat from the original predicted frozen values. However, updating the frozen predictions following each OMM with achieved values of e and ω provides considerably better agreement. The AOP exhibits the same general behavior (Fig. 20b).

The maximum deviations of observed (e, ω) values from the updated frozen predictions also correlate very well with β' variations. During periods of peak β' when the orbit is in full sun and $\beta' > 0$, the observed mean eccentricity is always less than the frozen value; this trend is reversed when $\beta' < 0$. Solar radiation pressure causes this behavior, as depicted in Fig. 21 for the 6-month period beginning March 1, 1994. For the three β' cycles included in this sample comparison, the mean eccentricity difference exhibits the same β'-dependent behavior. The maximum ω deviations from the updated frozen values are near $\beta' = 0$ when occultation periods are longest, resulting in the largest solar radiation pressure influences.

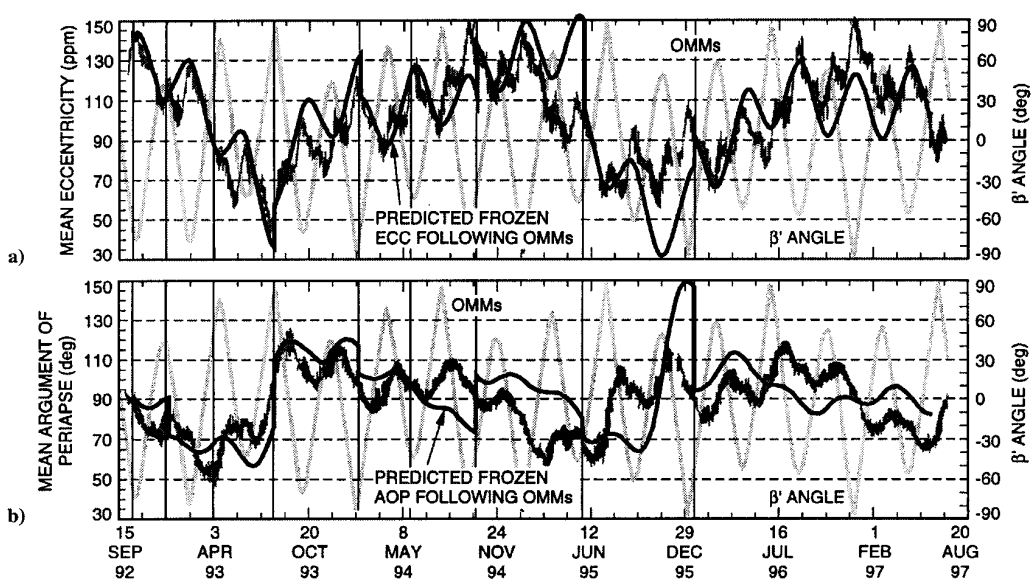

Fig. 20 Effects of maneuvers on the eccentricity vector (e, ω) parameters: a) mean eccentricity and b) mean AOP.

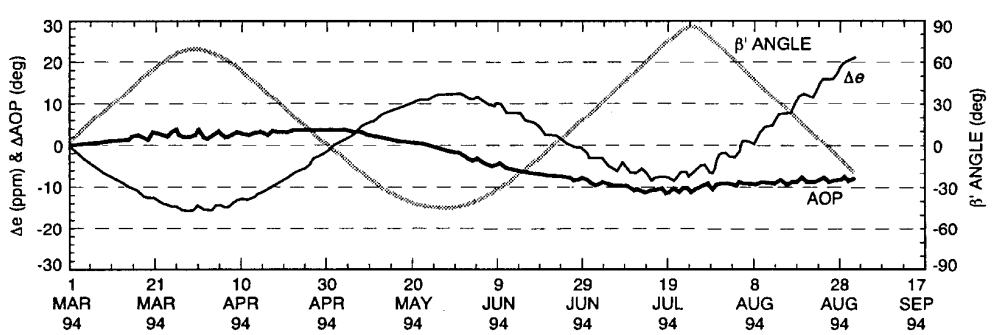

Fig. 21 Effects of solar radiation pressure on mean eccentricity and AOP.

The frozen orbit has been maintained since launch without requiring dedicated maneuvers. However, every effort has been made to decrease the mean eccentricity when performing OMMs. Although maneuver burns are constrained to occur over land to limit altimetry outages, which could result from possible attitude disturbances, cycle boundary locations near an orbit node (usually mid-South America) have allowed mean eccentricity to be slightly reduced or to remain nearly unchanged. The two exceptions were following OMM4 and OMM8 executed near orbit perigee over northern Canada and eastern Russia, respectively, to satisfy satellite pointing constraints during turns to and from the burn attitude. These two maneuvers modestly increased the postmaneuver mean eccentricity, as shown in Fig. 20a.

Variations in eccentricity Δe also affect ground-track equatorial crossings through variations in true anomaly Δf. For a near-circular orbit, $\Delta f = 2\Delta e \sin M$. For example, an eccentricity error of $\sim$10 ppm causes a maximum $\Delta f = 2\times10^{-5}$ rads, which is equivalent to an equatorial crossing timing error $\Delta t = \Delta f/n \approx 21$ ms. The amplitude of the corresponding equatorial longitude error $\Delta\lambda = \omega_e \Delta t \approx 10$ m. This modest longitude error systematically oscillates with expected variations in ω.

Ground-Track History

As of July 4, 1997, TOPEX/Poseidon had completed 176 ground-track repeat cycles (22,352 orbits) in the operational orbit. Only 95 nodal crossings ($\sim$0.4%) have been outside the $\pm$1-km ground-track control band. These excursions were voluntary, for the start of the first repeat cycle was declared before the ground track first entered the western control band and then crossed the eastern boundary before executing OMM1 on Oct. 12, 1992. The time of OMM1 was purposely delayed to provide additional observation and analysis time to characterize the influences of the newly discovered body-fixed forces on the predicted ground track and related maneuver design.

With the exception of the first, each OMM was executed as the ground track approached the eastern control boundary after the semimajor axis had decayed below a_o (see Figs. 7 and 22). These maneuvers are constrained to occur near the predetermined boundary between 10-day ground-track repeat cycles ($\pm$ one orbit) to prevent possible corruption of POD processes. The nominal strategy executes each OMM at the next-to-last cycle boundary before the ground track would exit the eastern control boundary. This conservative practice provides one backup opportunity still inside the control band if the nominal maneuver could not occur as planned. As can be seen from Fig. 22, the spacings between the most recent maneuvers are noticeably larger than for earlier OMMs. This performance is due to lower drag near the solar minimum and ongoing improvements in the prediction and use of the body-fixed forces.

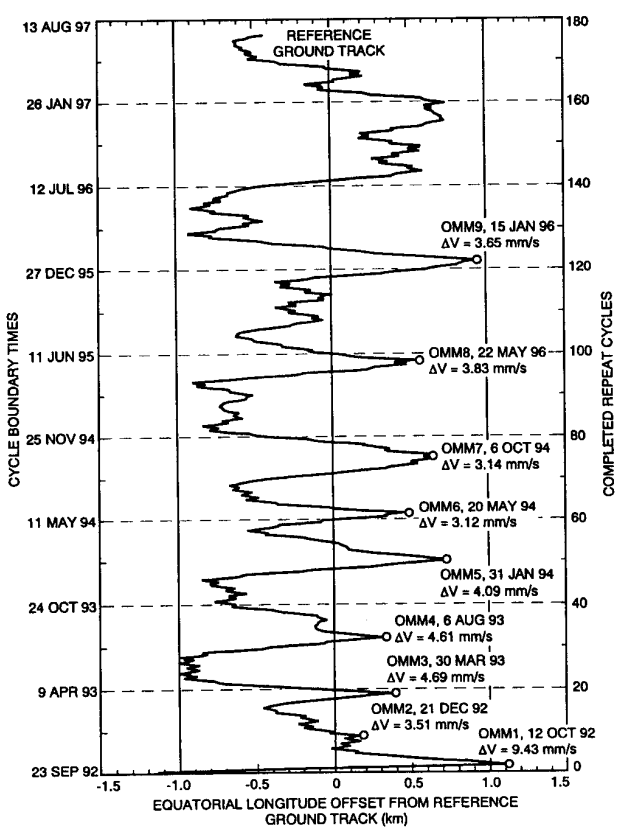

Fig. 22 TOPEX/Poseidon ground-track history through 176 repeat cycles.

Maneuver spacing and placement have sometimes been enhanced by modifying the nominal $\pm$15-deg β' limits governing entry into and out of the fixed yaw modes.[36] Margins in solar array and battery performance allow β' limits as large as $\sim$27 deg during fixed yaw periods near perihelion, being reduced to a minimum $\pm$15-deg limit when near aphelion. Modifying the duration of fixed yaw periods alters the net orbital boost or deboost levels to adjust the mean semimajor axis slowly and refine ground-track motion. A variation of this strategy selectively uses solar-array lead or lag positioning to refine semimajor axis control further. This technique has been successfully used since OMM9 (Jan. 15, 1996) to control the ground track without requiring propulsive maneuvers.

Distinct and important features in the ground-track behavior are the oscillations during the westernmost excursions between each OMM. The precise nature of these oscillations depends on the complex combination of time-dependent influences of lunar and solar gravity, atmospheric drag, radiation forces of body-fixed origin, and the current value of the mean semimajor axis. Drag forces can sometimes mask the effects of the other forces during periods of high solar activity, even at TOPEX/Poseidon altitude. However, the solar activity has been relatively low ($\bar{F}_{10.7} < 80\times10^{-22}$ W/m^2/Hz) during most of the mission. As a result, the influences of lunar and solar gravity have become more prominent, especially when the ground-track drift slows as the mean semimajor axis comes within a few meters of a_o. Under these conditions, third-body gravity forces tend to dominate ground-track behavior, causing periodic oscillations without significant net drift, e.g., Fig. 22.

Conclusions

The TOPEX/Poseidon operational orbit and ground-track behavior have been analyzed and interpreted. This process has been possible by employing precise mean elements computed using a new osculating-to-mean conversion technique that has demonstrated excellent stability (Table 3). The three most important orbital parameters are the semimajor axis, inclination, and eccentricity vector (e, ω). Analysis shows that precise knowledge and control of the mean semimajor axis is essential for effective ground-track control, whereas systematic variations in inclination and the eccentricity vector are acceptable without corrective maneuvers.

The mean semimajor axis variations result from a combination of atmospheric drag and radiation forces of body-fixed origin. Atmospheric drag always causes semimajor axis decay; the rate primarily depends on the solar flux level. The body-fixed forces induce either a boost or a deboost in the semimajor axis; the magnitude and direction depends on the satellite yaw-control mode. Isolation of the drag contributions to semimajor axis behavior would permit reconstruction of atmospheric density from which improved density modeling might be feasible. However, confident separation of semimajor-axis behavior into distinct drag and body-fixed components is not possible because both are along-track forces of comparable magnitude.

The orbit inclination and eccentricity vector parameters behaved as expected. The inclination exhibits periodic variations of less than $\pm$4 m deg about i_o owing almost entirely to lunar and solar gravitational perturbations. These deterministic forces have a significant effect on the satellite ground track but are easily compensated for when adjusting the mean semimajor axis to control the ground track. The eccentricity vector variations preserve the frozen orbit conditions. Analysis showed distinct, albeit small, changes in eccentricity when OMMs were executed even though the maneuver magnitudes were only 3–5 mm/s. Also, eccentricity variations

on the order of ±20 ppm were observed during orbit full-sun ($\beta' > 55.7$ deg) due to solar radiation pressure forces.

Orbit and ground-track maintenance activities are expected to continue essentially unchanged for the remainder of the extended mission, which has recently been approved through 2001. Should the satellite remain operational for several more years, expected increases in solar activity in 1998 will heighten the importance of atmospheric drag. As a result, the spacing between maneuvers could become more frequent, possibly as often as once every two to three months, compared with about twice annually during the recent period of low solar activity.

Jason, the successor French mission currently planned for launch in April 2000, will share the same reference orbit and repeat ground track with TOPEX/Poseidon to continue oceanographic investigations from space. Mission objectives and orbit control requirements similar to TOPEX/Poseidon will be retained. During early mission phases, Jason may fly in formation with TOPEX/Poseidon to help correlate independently acquired altimeter measurements. During this checkout period, the along-track separation between Jason and TOPEX/Poseidon may be controlled while both satellites remain within ±1 km of the reference ground track. Following this checkout period, TOPEX/Poseidon, with a sizable propellant margin, may be retargeted to offset the spacing from Jason by 5 days, thereby providing oceanographic data sets for two separate 10-day repeat cycles or, if combined, the equivalent of a single 5-day repeat cycle.

Acknowledgment

The research described in this paper was carried out by the Jet Propulsion Laboratory, California Institute of Technology, under contract with NASA.

References

[1]Frautnick, J. C., and Cutting, E., "Flight Path Design Issues for the TOPEX Mission," AIAA Paper 82-0202, Jan. 1982.

[2]Farless, D. L., "The Application of Periodic Orbits to TOPEX Mission Design," *Advances in the Astronautical Sciences*, Vol. 58, Pt. 1, 1986, pp. 13–35.

[3]Bhat, R. S., Frauenholz, R. B., and Cannell, P. E., "TOPEX/Poseidon Orbit Maintenance Maneuver Design," *Advances in the Astronautical Sciences*, Vol. 71, Pt. 1, 1989, pp. 645–670.

[4]Tapley, B. D., Ries, J. C., Davis, G. W., Eanes, R. J., Schutz, B. E., Shum, C. K., Watkins, M. M., Marshall, J. A., Nerum, R. S., Putney, B. H., Klosko, S. M., Luthcke, S. B., Pavlis, D., Williamson, R. G., and Zelensky, N. P., "Precision Orbit Determination for TOPEX/Poseidon," *Journal of Geophysical Research*, Vol. 99, No. C12, 1994, 24,383–24,404.

[5]Marshall, J. A., Zelensky, N. P., Klosko, S. M., Chinn, D. S., Luthcke, S. B., Rachlin, K. E., and Williamson, R. G., "The Temporal and Spatial Characteristics of the TOPEX/Poseidon Radial Orbit Error," *Journal of Geophysical Research*, Vol. 100, No. C12, 1995, pp. 25,331–25,352.

[6]Chobotov, and Vladimir, A., *Orbital Mechanics*, AIAA Education Series, AIAA, Washington, DC, 1991, pp. 291–296.

[7]Dickerson, K. G., Herder, R. W., Glass, A. B., and Cooley, J. L., "Application of Altitude Control Techniques for Low Altitude Earth Satellites," *Journal of the Astronautical Sciences*, Vol. 26, No. 2, 1978, pp. 129–148.

[8]Cutting, E., Born, G. H., and Frautnick, J. C., "Orbit Analysis for SEASAT-A," *Journal of the Astronautical Sciences*, Vol. 26, No. 4, 1978, pp. 315–342.

[9]Herder, R. W., Cullen, M. F., and Glass, A. B., "Description and Application of the Frozen Orbit Concept," Computer Sciences Corp., CSC/TM-79/6089, Lanham–Seabrook, MD, Aug. 1979, pp. 3.1–3.21.

[10]Smith, J. C., "Analysis and Application of Frozen Orbits for the TOPEX Mission," AIAA Paper 86-2069, Aug. 1986.

[11]Doll, C. E., Mistretta, G., and Hart, R., "Accuracy Assessment of TDRSS-Based TOPEX/Poseidon Orbit Determination Solutions," *Advances in the Astronautical Sciences*, Vol. 85, Pt. 1, 1994, pp. 123–142.

[12]Kozai, Y., "The Motion of a Close Earth Satellite," *Astronomical Journal*, Vol. 64, No. 1274, 1959, pp. 367–377.

[13]Brouwer, D., "Solution of the Problem of Artificial Satellite Theory Without Drag," *Astronomical Journal*, Vol. 64, No. 1274, 1959, pp. 378–397.

[14]Guinn, J. R., "Periodic Gravitational Perturbations for Conversion Between Osculating and Mean Orbit Elements," *Advances in the Astronautical Sciences*, Vol. 76, Pt. 2, 1991, p. 1470.

[15]Guinn, J. R., Bhat, R. S., Vincent, M. A., and Konopliv, A. S., "Conversion of Classical Orbital Elements," NASA Tech Briefs, COSMIC NPO-18741/18796, Vol. 18, No. 12, 1994, pp. 58–60.

[16]Nerum, R. S., Lerch, F. J., Marshall, J. A., Pavlis, E. C., Putney, B. H., Tapley, B. D., Eanes, R. J., Ries, J. C., Schutz, B. E., Shum, C. K., Watkins, M. M., Klosko, S. M., Chan, J. C., Luthcke, S. B., Patel, G. B., Pavlis, N. K., Williamson, R. G., Rapp, R. H., Biancale, R., and Nouel, F., "Gravity Model Development for TOPEX/ Poseidon: Joint Gravity Models 1 and 2," *Journal of Geophysical Research*, Vol. 99, No. C12, 1994, pp. 24,421–24,447.

[17]Tapley, B. D., Watkins, M. M., Ries, J. C., Davis, G. W., Eanes, R. J., Poole, S. R., Rim, H. J., Lerch, F. J., Schutz, B. E., Shum, C. K., Nerum, R. S., Marshall, J. A., Klosko, S. M., Pavlis, N. K., and Williamson, R. G., "The Joint Gravity Model 3," *Journal of Geophysical Research*, Vol. 101, No. B12, 1996, pp. 28,029–28,049.

[18]Escobal, P. R., *Methods of Orbit Determination*, Kreiger, Malabar, FL, 1976, p. 381.

[19]Frauenholz, R. B., and Shapiro, B. E., "The Role of Predicted Solar Activity in TOPEX/Poseidon Orbit Maintenance Maneuver Design," *Advances in the Astronautical Sciences*, Vol. 76, Pt. 2, 1992, pp. 1152–1170.

[20]Frauenholz, R. B., Hamilton, T. W., Shapiro, B. E., and Bhat, R. S., "The Role of Anomalous Satellite-Fixed Accelerations in TOPEX/Poseidon Orbit Maintenance," *Advances in the Astronautical Sciences*, Vol. 85, Pt. 1, 1994, pp. 83–102.

[21]Richter, R., "Radiation Forces Acting on the TOPEX/Poseidon Spacecraft Along the Velocity Vector Due to the Solar Array—Initial Results," Jet Propulsion Lab., JPL IOM 3544-TOP-93-004, California Inst. of Technology, Pasadena, CA, July 1993 (internal document).

[22]Richter, R., "Determination of Satellite Acceleration," Jet Propulsion Lab., JPL IOM 3544-TOP-93-007, California Inst. of Technology, Pasadena, CA, Sept. 1993 (internal document).

[23]Richter, R., "Radiation Forces During Sinusoidal Yaw Steering for Three Solar Array Bias Angles," Jet Propulsion Lab., JPL IOM 3544-TOP-93-014, California Inst. of Technology, Pasadena, CA, Nov. 1993 (internal document).

[24]Cangahuala, L. A., Christensen, E. J., Graat, E. J., Williams, B. G., and Wolff, P. J., "TOPEX/Poseidon Precision Orbit Determination, 'Quick-Look' Operations and Orbit Verification," *Advances in the Astronautical Sciences*, Vol. 89, Pt. 2, 1995, pp. 1641–1653.

[25]Jacchia, L. G., "Static Diffusion Models of the Upper Atmosphere with Empirical Temperature Profiles," Smithsonian Astrophysical Observatory, Special Rept. 170, Cambridge, MA, Dec. 1964, pp. 1–15.

[26]Jacchia, L. G., "Atmosphere Models in the Region 110 to 2000 km," *CIRA-72 COSPAR International Reference Atmosphere*, Committee for the COSPAR International; Reference Atmosphere (CIRA) of COSPAR (Committee on Space Research) Working Group 4, Akadamie–Verlag, Berlin, 1972, pp. 227–260.

[27]Jacchia, L. G., "Thermospheric Temperature, Density, and Composition: New Models," Smithsonian Astrophysical Observatory, Special Rept. 375, Cambridge, MA, March 1977, pp. 1–64.

[28]Roberts, C., "An Analytic Model for Upper Atmosphere Densities Based Upon Jacchia's 1970 Models," *Celestial Mechanics*, Vol. 4, 1971, pp. 368–377.

[29]Barlier, F., Berger, C., Falin, J. L., Kockarts, G., and Thuillier, G., "Comparisons Between Various Semi-Empirical Thermospheric Models of the Terrestrial Atmosphere," Belfisch Instituut voor Ruimte-Aëronomie, Brussels, Belgium, 1979.

[30]Kaula, W. M., "Development on the Lunar and Solar Disturbing Functions for a Close Satellite," *Astronautical Journal*, Vol. 67, June 1962, pp. 300–303.

[31]Bhat, R. S., and Cannell, P. E., "Effects of Variation of Mean Orbital Parameters on Ground Track Pattern and Repeatability," Jet Propulsion Lab., JPL IOM 314.5-1330, California Inst. of Technology, Pasadena, CA, Jan. 1989 (internal document).

[32]Bhat, R. S., and Shapiro, B. E., "TOPEX/Poseidon Ground Track Control Using Lead/Lag Strategy," Jet Propulsion Lab., JPL IOM FOS 96-037, California Inst. of Technology, Pasadena, CA, June 1996 (internal document).

[33]Bhat, R. S., and Shapiro, B. E., "Performance of TOPEX/Poseidon Orbit Maintenance Maneuver-9," Jet Propulsion Lab., JPL IOM FOS 96-017, California Inst. of Technology, Pasadena, CA, Feb. 1996 (internal document).

[34]Bhat, R. S., Shapiro, B. E., and Frauenholz, R. B., "TOPEX/Poseidon Orbit Acquisition Maneuver Sequence," *Advances in the Astronautical Sciences*, Vol. 85, Pt. 1, 1994, pp. 103–122.

[35]Shapiro, B., "Phase Plane Analysis and Observed Frozen Orbit for the TOPEX/Poseidon Mission," *Advances in the Astronautical Sciences*, Vol. 91, 1996, pp. 853–872.

[36]Shapiro, B. E., Bhat, R. S., and Frauenholz, R. B., "Using Anomalous Along-Track Forces to Control the TOPEX/Poseidon Ground Track," *Advances in the Astronautical Sciences*, Vol. 87, Pt. 2, 1994, pp. 799–812.

F. H. Lutze Jr.
Associate Editor